Tuning a Charge Impurity in Graphene: from Cloaking to Supercriticality

Adina Luican-Mayer[1], Maxim Kharitonov[1], Guohong Li[1], ChihPin Lu [1], Ivan Skachko[1], Alem-Mar B. Goncalves[1], K. Watanabe[2], T. Taniguchi[2] and Eva Y. Andrei[1]

[1]Department of Physics and Astronomy, Rutgers University, Piscataway, NJ 08854, USA

[2] National Institute for Materials Science, 1-1 Namiki, Tsukuba, 305-0044, Japan

Atomic orbitals become unstable when the nuclear charge exceeds a critical value, comparable to the inverse fine structure constant, at which point relativistic effects cause electrons to fall into the nucleus [1,2]. Accessing this critical regime where new physics comes into play requires the creation of ultra-heavy nuclei which do not exist in nature. Here we demonstrate that in graphene[3-5] it is possible to explore this regime by using an isolated charged impurity as the nucleus of an artificial atom[6-9] together with a magnetic field and a gate voltage which define the electronic orbitals. Using scanning tunneling microscopy and spectroscopy in an ultra-clean graphene sample we show that the effective charge of the impurity can be tuned from the subcritical to the supercritical regime by controlling the occupancy of the electronic states (Landau levels) with the gate voltage. At low occupancy strong screening by the conduction electrons cloaks a positively charged impurity rendering it essentially invisible. As the impurity strengthens with increased occupancy the orbital degeneracy of nearby electronic states is lifted leading to fine splitting of the energy levels. At full occupancy where the impurity is unscreened it enters the supercritical regime which is identified by the appearance of a series of localized states in the negative energy sector. Our findings show that the magnetic field makes it possible to tune the strength of impurities in graphene from subcritical to supercritical providing unprecedented access to the regime of Coulomb criticality.

The critical charge of atomic nuclei, Z_c , is defined by $Z_c\alpha = 1$ where α=1/137 is the fine structure constant. In graphene where the effective fine structure constant $\alpha_g = \frac{1}{\kappa}\frac{c}{v_F}\alpha$ is much larger, the critical regime can in principle be accessed for relatively modest values of Z [6,7] . Here κ is the dielectric constant, *c* the speed of light and v_F the Fermi velocity. In the experiments reported here a magnetic field and a gate voltage were employed to tune the effective charge of an impurity which served as the nucleus in artificial atom formed in a high quality graphene sample.

Graphene, being a two dimensional (2D) material in which the Fermi energy can be controlled by gating, provides a unique playground for elucidating the effect of charged impurities [6-13]. Because of their ultra-relativistic nature electrons in graphene cannot be bound by a charged impurity. This situation changes in the presence of a magnetic field, *B*, normal to the graphene layer when the electrons occupy quantized Landau levels[14-16] (LL) which confine them to orbits around the impurity. The impurity can thus be viewed as the nucleus in an artificial atom with the LL index playing the role of the principal quantum number. Furthermore, lifting of the LL orbital degeneracy in the presence of the impurity is analogous to fine splitting of atomic energy levels. The effective nuclear charge in this artificial atom is determined by the screening properties of the conduction electrons which can be controlled by tuning the position of the Fermi energy with respect to the LLs. When the Fermi energy is placed within a LL the response is metallic and the screening strong, while it is insulating when the Fermi energy is in a gap between LLs. As we will show, in the metallic state the impurity becomes practically invisible due to efficient screening by conduction electrons, while in the insulating state the unscreened impurity becomes supercritical and significantly alters its electronic environment.

The LL sequence in graphene is given by:

$$E_N = \pm\hbar\frac{v_F}{l_B}\sqrt{2|N|}\text{ , N=0, ±1,±2, …} \qquad (1)$$

where $\hbar$ is the reduced Planck constant, $l_B = \sqrt{\hbar/eB}$ the magnetic length, -*e* the electron charge, N the LL index, and +(-) refers to electron (hole) states. The LL sequence gives rise to distinctive peaks in the density of states (DOS) which are readily observed with scanning tunneling microscopy (STM) and spectroscopy (STS), employed in our experiments[5,17-19].

Graphene samples were prepared by mechanical exfoliation from analyzer-grade HOPG (highly oriented pyrolytic graphite) and deposited on a substrate (SiO_2 or BN) capping a doped

Si backgate[18] . The best sample quality was attained by using two superposed graphene layers twisted away from Bernal stacking by a large angle (G/G/SiO_2 and G/G/BN in Figure 1). This ensures minimal coupling to the substrate and between layers so that the LL spectrum of single layer graphene is preserved [19] (supplementary-material). We then employed LL spectroscopy to locate the impurity and to characterize it at low temperatures (supplementary-material). Figures 2(a,b) show the STM topography of an isolated impurity found in the G/G/SiO_2 sample and the LL spectrum taken far from the impurity. Fitting the field and level-index dependence of the LL energies to Equation 1 confirms the single-layer nature of the spectrum with v_F=1.1 x10^6m/s, consistent with measurements of graphene on insulating substrates[3]. To visualize the effect of the impurity we measured constant energy differential-conductance (*dI/dV)* maps in its vicinity for energies in the center of a LL and in the gap between LLs, Figure 2(c, f). The maps are radially symmetric consistent with a charged impurity at the center.

We next studied the effect of LL occupancy (filling) by tuning the gate voltage, V_g , to progressively fill the LLs. The LL filling factor is ν=n/n_0(B) where $n \sim 7 \times 10^{10}\, V_g\ (V)\ [cm^{-2}]$ is the carrier density and $n_0(B) = g_l g_v g_s \frac{Be}{2\pi\hbar}$ is the degeneracy/area of the LL. Here $g_l = g_v = g_s = 2$ represent the layer, valley and spin degeneracy respectively. Placing the STM tip far from the impurity we find that as V_g is swept the LL peaks produce a distinctive step-like pattern seen as bright traces in the intensity map of Figure 3(b) [18,20]. Each step consists of a nearly horizontal plateau separated from its neighbors by steep slopes. The separation between steep segments, $\Delta V_g \approx 28V$, gives the LL degeneracy $\sim 2\times10^{12}[\mathrm{cm}^{-2}]$ for B=10T, as expected for this double-layer sample [21,22]. The plateau indicates that the Fermi-energy remains pinned within a narrow energy band around the center of the LL until the plateau states are filled. Subsequently, a further increase in V_g populates the sparse states in the gap producing the steep slopes. We note that although STM explores only a small area of the sample, the gate-voltage dependence reflects all the available states, including those outside the field of view, because the gate covers the entire sample.

To explore the influence of the impurity on the LLs we follow in Figure 3(c) the spatial evolution of the LL spectra as a function of V_g. We note that at certain values of V_g the spectra near the impurity are distorted, with the N=0 level (and to a lesser extent higher-order levels)

shifting down in energy. The downshift is consistent with an attractive potential produced by a positively-charged impurity. Its strength, as measured by the distortion of the N=0 LL, reveals a close correlation with LL filling: at low filling, V_g= -10V, the distortion is almost absent so the impurity is effectively masked. The distortion reaches its maximum value when the plateau-states are fully occupied at V_g=+7V, -25V. In this regime the N=0 level shifts by as much as ~0.1 eV indicating that the effect would survive at room temperature. We emphasize that the spectral distortion is only seen near the impurity. Far away from it the spectrum is spatially uniform.

We attribute the variation in the strength of the impurity potential to the screening properties of the 2D electron system. For a positively charged impurity and almost empty LLs, both filled and empty states necessary for virtual electron transitions are readily available near the impurity, which leads to substantial screening, Figure 3(d). In contrast for almost filled LLs all states near the impurity are occupied, rendering local screening inefficient. The situation would be reversed for a negatively charged impurity.

Remarkably, when screening is minimal (V_g=+7V,+5V,-25V) the N=0 LL does not shift smoothly, but splits into a series of discrete spectral lines in the immediate vicinity of the impurity. As shown in Figure 4(a, b) the evolution of the spectra as one moves away from the center of the N=0 LL splits into a progression of peaks. Starting with a single peak at the center of the impurity, it evolves into a double peak and then a triplet at distances ~ 0,13, 20 nm from the center.

The effect of the impurity can be understood by considering the quantum mechanical motion of an electron in graphene. In one valley and for each spin projection, the two-component wave-function $\psi = (\psi_A, \psi_B)^T$ satisfies an effective Dirac Hamiltonian:

$$\widehat{H}\psi = E\psi\,, \widehat{H} = \widehat{H}_0 + U(r), \widehat{H}_0 = v_F\boldsymbol{\sigma}(\boldsymbol{p} - e\boldsymbol{A}) \qquad (2)$$

Here, $\widehat{H}_0$ corresponds to the case without the impurity, $\boldsymbol{\sigma}$ =(σ_x,σ_y) are the Pauli matrices in the AB sublattice space**,** $\boldsymbol{p} = -i\hbar\boldsymbol{\nabla}$ is the momentum operator, $\mathbf{B} = \boldsymbol{\nabla}\mathrm{x}\boldsymbol{A}$ **,** and $\boldsymbol{A}$ is the vector potential. We assume a radially symmetric potential U(r) of an impurity located at r = 0, and neglect the Zeeman Effect. In the symmetric gauge $\boldsymbol{A} = \frac{1}{2}[\boldsymbol{B} \times \boldsymbol{r}]$ the eigenstates are characterized by the orbital quantum-number *m*. Solving the eigenvalue problem for $\widehat{H}_0$ yields the unperturbed LL spectrum E_N of Equation (1), and the eigenfunctions ${\psi^0}_{NmA}(r)$,

$\psi^0{}_{NmB}(r)$, where $m \geq -|N|$ (supplementary-material). Since E_N are independent of m, the LLs have an infinite orbital degeneracy (for an infinite sample).

The impurity lifts the orbital degeneracy and the eigen-energies split into sublevels, E_{Nm}. To illustrate impurity-induced orbital splitting we numerically solved the problem for a Coulomb potential $U(r) = \frac{Ze^2}{\kappa 4\pi\varepsilon_0}\frac{1}{r}$ of an impurity in the subcritical regime with charge Z, where ε_0 is the permittivity of free space (supplementary-material). The impurity potential introduces an *m*-dependent downshift in energy which is largest for E_{00}, Figure 4(c). For a direct comparison with the STS data we calculate the local tunneling DOS using a phenomenological model with LLs of finite linewidth γ :

$$D(E,\boldsymbol{r}) = 4\sum_{Nmi}\delta_\gamma(E - E_{Nm})\,\psi^\dagger{}_{Nmi}(r)\,\psi_{Nmi}(r). \quad (3)$$

Here, *i* is the sublattice index and $\delta_\gamma(E - E_{Nm}) = \gamma/[\pi((E - E_{Nm})^2 + \gamma^2)]$ represents the broadened LL. The discreteness of the spectrum E_{Nm} around a given *m* can be resolved in the experimental $D(E,r)$, if $\gamma \lesssim \Delta E_{Nm}$, where ΔE_{Nm} is the separation between adjacent levels. For $\gamma \gtrsim \Delta E_{Nm}$ the peaks of adjacent (in space and energy) states overlap and merge into a continuous line causing the measured $D(E,r)$ to display "bent" LLs[23-26].

Comparing the simulated DOS with the data, Figure 4(a) we can attribute the observed discrete spectral lines within the N=0 level to states with $= 0, 1, 2$. For partial filling, ($Vg = -10V, -5V, 0$ V), as screening becomes more efficient the sublevels merge into continuous lines of bent LLs even for N=0. Thus the capability to tune the strength of the impurity potential allows us to trace the evolution between the discrete and the quasi-continuous regimes.

A rough estimate of the impurity strength can be obtained by using first order perturbation theory to fit the observed energy shift for N=m=0, $E_{00} \approx \frac{Ze^2}{\kappa 4\pi^{1/2}\varepsilon_0 l_B}$. Fitting this expression to the observed shift, E_{00} ~ 0.1eV at V_g = +7V gives $Z/\kappa \sim 0.4$. Repeating the procedure for the shifts $E_{00}(V_g)$ at other values of V_g we obtain the filling dependence of Z/κ plotted in Figure 3(e). In the 2D Dirac equation applicable for graphene [6,7], $Z_c\alpha_g$ =1/2, and the supercritical regime is reached for $Z\alpha_g = 2.2\frac{Z}{\kappa} \geq \frac{1}{2}$ (for v_F=1.1 x10^6m/s) . Thus at V_g=+7V, where $Z/\kappa = 0.4$, the impurity is well into the supercritical regime. As filling decreases and screening becomes more efficient the impurity weakens eventually crossing into the subcritical

regime. For V_g=+5V where $Z/\kappa = 0.3$, the impurity is still supercritical but at V_g=-10V where $Z/\kappa = 0.07$ it is subcritical. As seen in Figures 3(c), 4(d) the spectra in the supercritical regime (V_g=+7V, +5V,-25V) are characterized by the conspicuous appearance of negative energy states localized in the immediate vicinity of the impurity which override the LLs. According to theory, the appearance of negative energy states outside the LL sequence signifying the breakdown of electronic orbits at the charged impurity, is the hallmark of the supercritical regime [6,7,15,27]. These states are the equivalent of the negative energy resonances predicted to occur in atoms with a super-critical nuclear charge.

This work demonstrates that in ultra-clean graphene an isolated impurity in the presence of a magnetic field behaves as the nucleus in a multi-level tunable artificial atom. The effective charge of this nucleus can be continuously tuned *in-situ* by varying the magnetic field and gate voltage, from the subcritical regime to the regime of Coulomb criticality where new physics associated with the collapse of electronic orbits comes into play.

Acknowledgements

Funding was provided by Lucent (A.L), DOE-FG02-99ER45742 (E.Y.A and G.L) , NSF DMR 1207108 (I.S., C.P.L) , DOE DE-FG02-99ER45790 (M. K.), Brazilian agency Capes BEX 5115-09-4 (A.M.B.G). We wish to thank M. Aronson for the monochromator grade HOPG crystal.

Figures

Figure 1. Graphene samples for gated STM/STS measurements. (a) Schematics of gated graphene device. The region labeled G+G represents two stacked graphene layers. (b) Optical micrograph showing graphene samples deposited on high quality substrates of 300nm thick chlorinated SiO_2 capping a doped Si backgate . In G/G/SiO_2 the stacked layers are deposited directly on SiO_2 while in G/G/BN/SiO_2 they are deposited on an exfoliated flake of h-BN above SiO_2. (c) STM topography images of the two sample regions, G/G/SiO_2 (left panel) and G/G/BN/SiO_2 (middle panel). Right panel: Line cuts from the STM topography images in the left and middle panels show that the typical corrugation height on the h-BN substrate is more than one order of magnitude lower than on SiO_2 consistent with previous reports [28]. Map sizes 80x80nm^2.

Figure 2. Landau level and differential tunneling-conductance maps, dI/dV , near an isolated impurity. (a) STM topography showing an area in sample G/G/SiO_2 that contains an isolated impurity (V_g=0V, V_{Bias}=250mV, I_t=20pA). (b) STS spectrum at B = 10 T for V_g =0V shows quantized LLs for N=0,±1, ,±2, ±3, ±4. The spectrum was taken at the position indicated by the circle in panel (a). STS spectra are obtained by measuring the dependence of dI/dV on the tip-sample bias voltage, $V = (E - E_F)/e$, where E is the energy measured relative to the Fermi-level, E_F. dI/dV is proportional to the local DOS, $D(E,\mathbf{r})$, at the tip position $\mathbf{r}$. (c) dI/dV maps at B=10T and V_g=0V of the area in (a). (d) STM topography of single layer graphene on chlorinated SiO_2. (e) LL spectrum at B=12T taken on the sample s in (d) at the position indicated by the circle. (f) dI/dV maps at B=12T for the area in (d). Left panel: for energies within the gap the DOS is localized on the impurity while for energies near the center of the LL (right panel) the DOS is delocalized and avoids the impurity. Scale bars 20nm; Map sizes 80x80 nm^2.

Figure 3. Screening by populating Landau levels. (a) Schematic DOS and LL sequence in graphene. The area below the Fermi energy (E=0), chosen to coincide with the charge neutrality point, represents occupied states, and above it are empty states. (b) Intensity map of LL spectra at 10T as a function of gate voltage taken at the position indicated by the circle in Figure 2(a). The dashed lines indicate the gate voltages at which the spectra in (c) were taken. The width of the N=0 plateau, $\Delta V_g \approx 24V$, and its energy range (~40mV) indicates that ~ 85% of the states in a LL are concentrated in a narrow band whose energy width is ~30% of the LL spacing. The

remaining states are spread over a wider energy range in the gap between LLs. (c) LL maps across the impurity in Figure 2(a) for indicated gate voltages. The distortion of the LL sequence by the impurity potential is strongest for almost fully occupied plateau states (V_g =+7V, +5V,-25V). As occupation decreases the distortion weakens until it becomes almost invisible at V_g = -10V. Scale bars l_B(10T) = 8.2nm. (d) Left panel: illustration of the local screening properties as a function of doping. At low filling (top) virtual transitions (indicated by arrows) between filled and empty states (red dots are electrons) occur in the vicinity of positively charged impurities but not near negatively charged ones leading to strong screening for the former. For almost full levels (bottom) the situation is particle-hole reversed. Right panel: the particle-hole asymmetry of the local screening properties is reflected in $D_S(E) = \int d^2r D(E,\boldsymbol{r})/S$, the DOS averaged over a finite-size region S, around a positively charged impurity. $D_S(E)$ is particle-hole asymmetric , unlike the DOS far from an impurity, reflecting the asymmetry of the local screening. The situation is reversed for a negatively charged impurity. (e) Evolution of the effective impurity charge (left axis) with LL occupancy indicated on the top axis by the filling factor ν. The effective charge increases monotonically with occupancy reaching its largest value for full LLs. Supercritical behavior identified by the appearance of negative energy peaks outside the LL sequence sets in above $Z\alpha_g$~0.5 marked by the dashed line.

Figure 4. Lifting the orbital degeneracy of LLs and supercrticality. (a) Top: Same as Figure 3c for V_g = +7V. Bottom: calculated probability densities for states ψ_{0m} with m=0,1,2 are consistent with the spatial distribution of the discrete spectral lines in the top panel. (b) dI/dV spectra represent line cuts on the map in (a) at the positions indicated by the dashed lines. A, B and C are taken at distances of 0nm, 13nm and 20nm from the center of the impurity corresponding to states with N=0 and m=0,1,2 respectively. States with higher m, less affected by the impurity, are not resolved. Similarly, the discreteness is not resolved for $N \neq 0$, consistent with the larger extent of the wavefunctions. (c) Left panel: simulated spectrum near an impurity obtained by solving equation 2 for a Coulomb impurity with β=0.4 illustrate the general properties of the solution: The level spacing is largest for eigenfunctions that are localized in the immediate vicinity of the impurity, i.e., for the lowest *m* and decreases with increasing m and/or N, as the extent of the wave-function increases. With increasing *m* the levels approach the unperturbed LLs. Right panel: simulated DOS near an impurity shows LL splitting due to lifting the orbital degeneracy. Linewidth $\gamma = 0.05\hbar v_F/l_B$. The discreteness of the spectrum is resolved for the

lowest Landau levels $N = 0, \pm 1$ consistent with the experimental map in (a). Red lines represent the calculated energies, E_{Nm} shown in the left panel. (d) Supercriticality. Top panel: LL spectra as a function of position along the line traversing the impurity for the data in Figure 3(c) at V_g=+7V. Spectra at different positions are offset vertically for clarity. Bottom curve corresponds to position marked 0nm and top curve at 85nm in Figure 3(c). The horizontal arrow indicates the center of the impurity. The pronounced peaks within the dashed circle indicate the appearance of negative energy resonances expected in the supercritical regime. Bottom panel: same as top panel but for V_g=-10V where the impurity is in the subcritical regime and the negative energy resonances are absent.

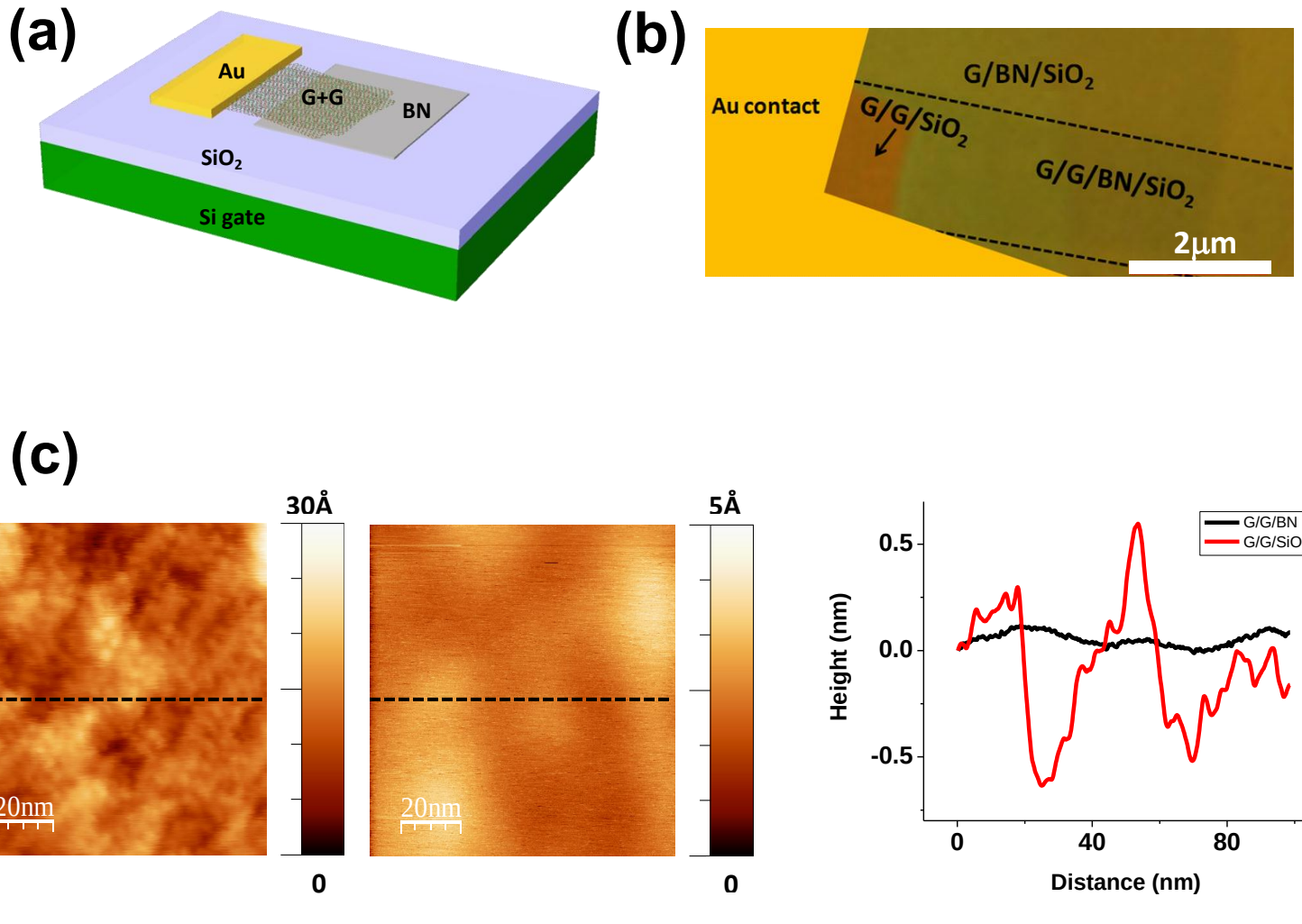
(a)
Au
G+G
BN
SiO2
Si gate
(b)
Au contact
G/BN/SiO2
G/G/SiO2
G/G/BN/SiO2
2μm
(c)
30Å
5Å
20nm
20nm
0
0
G/G/BN
G/G/SiO2
Height (nm)
0.5
0.0
-0.5
0
40
80
Distance (nm)

Figure 1

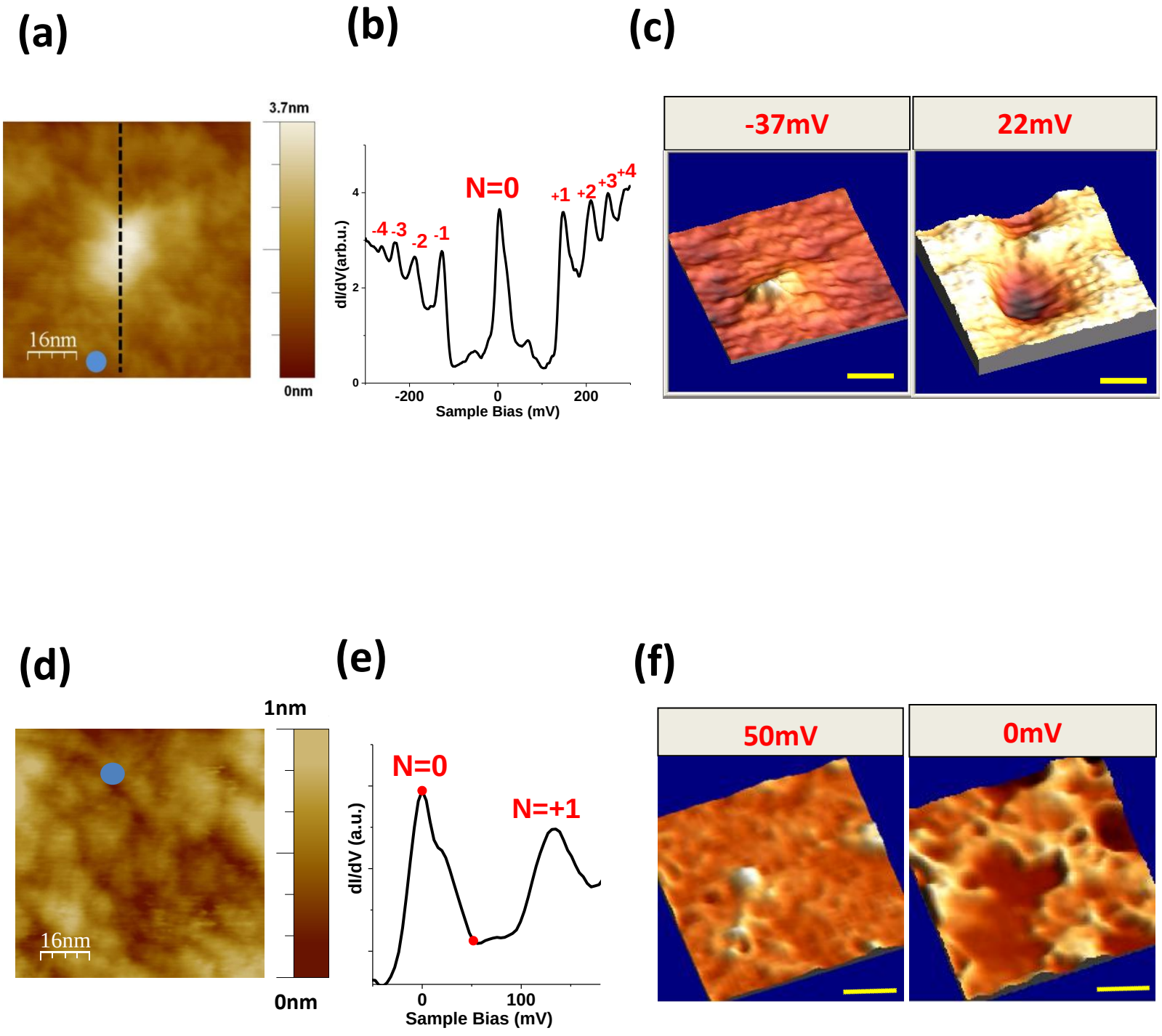
(a)
(b)
(c)
3.7nm
0nm
16nm
N=0
-4
-3
-2
-1
+1
+2
+3
+4
dI/dV(arb.u.)
Sample Bias (mV)
-37mV
22mV
(d)
(e)
(f)
1nm
0nm
16nm
N=0
N=+1
dI/dV (a.u.)
Sample Bias (mV)
50mV
0mV

Figure 2

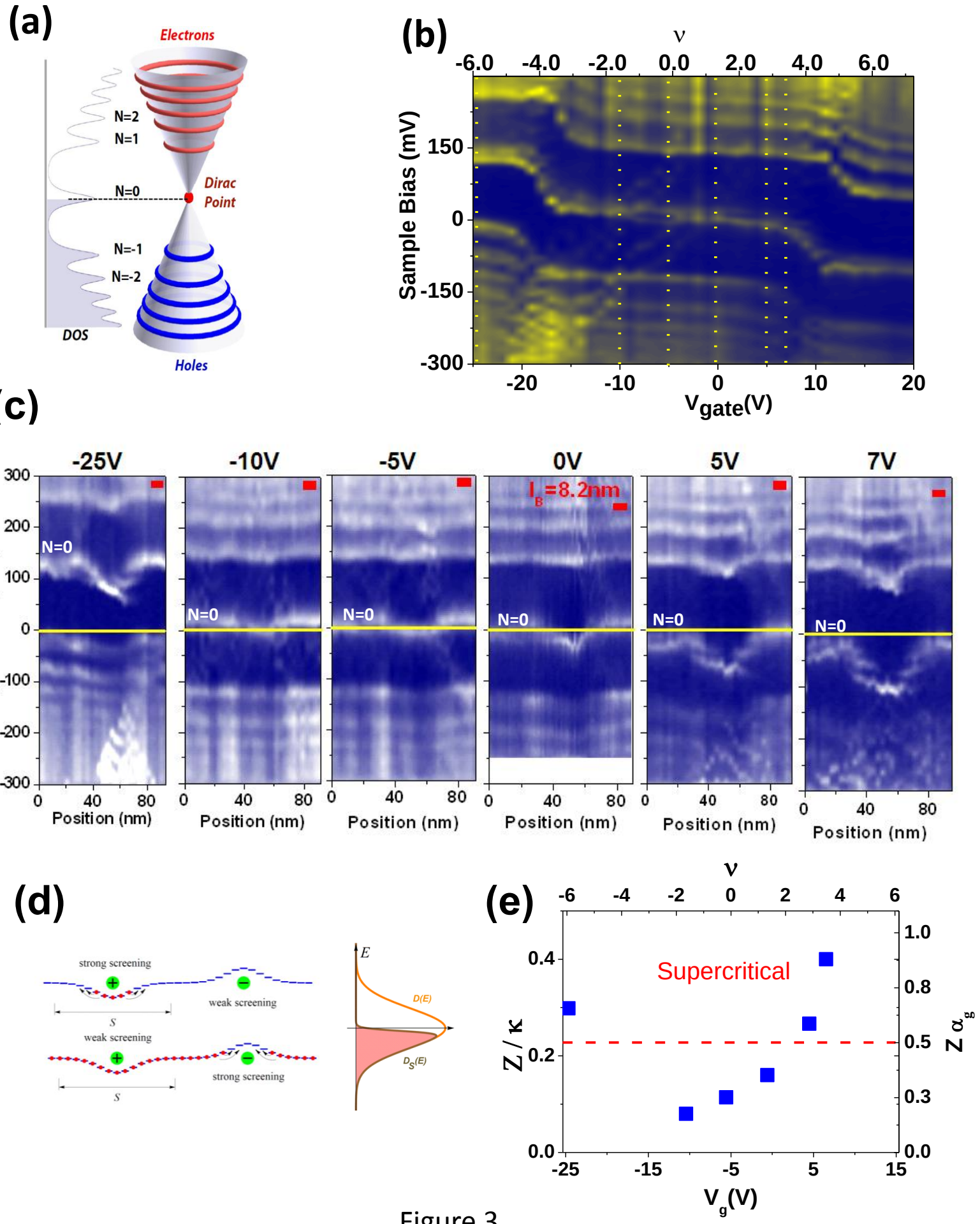
(a)
Electrons
N=2
N=1
N=0
Dirac Point
N=-1
N=-2
DOS
Holes
(b)
ν
-6.0 -4.0 -2.0 0.0 2.0 4.0 6.0
Sample Bias (mV)
150
0
-150
-300
-20 -10 0 10 20
Vgate(V)
(c)
-25V
-10V
-5V
0V
5V
7V
Sample Bias (mV)
300
200
100
0
-100
-200
-300
N=0
l_B=8.2nm
0 40 80
Position (nm)
(d)
strong screening
weak screening
S
weak screening
strong screening
S
E
D(E)
D_S(E)
(e)
ν
-6 -4 -2 0 2 4 6
Supercritical
Z / κ
0.0
0.2
0.4
Z α_g
0.0
0.3
0.5
0.8
1.0
-25 -15 -5 5 15
V_g(V)

Figure 3

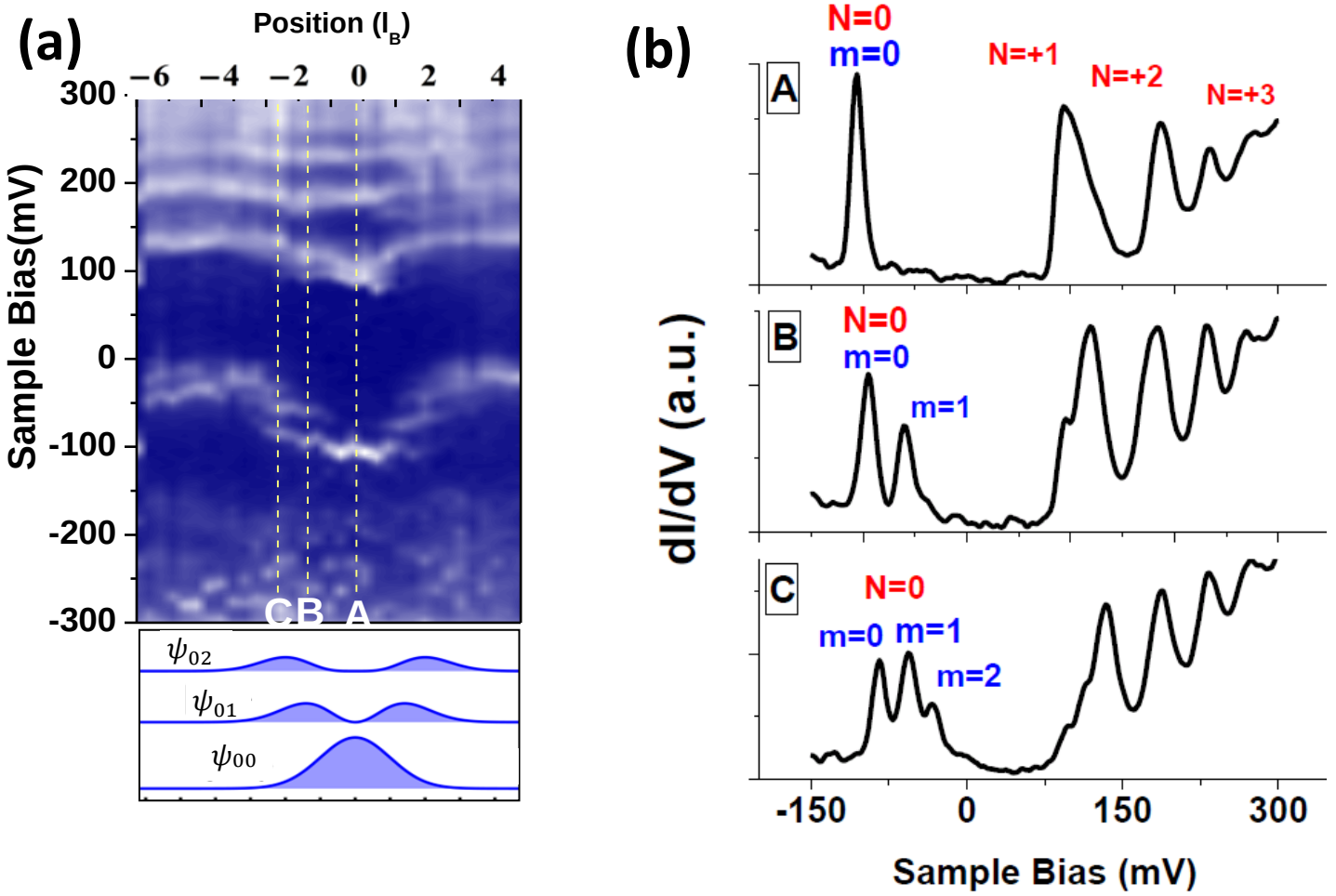
(a)
Position (l_B)
−6 −4 −2 0 2 4
300
200
100
0
-100
-200
-300
Sample Bias(mV)
CB A
ψ_{02}
ψ_{01}
ψ_{00}
(b)
N=0
m=0
N=+1
N=+2
N=+3
A
N=0
m=0
m=1
B
N=0
m=0 m=1
m=2
C
dI/dV (a.u.)
-150 0 150 300
Sample Bias (mV)

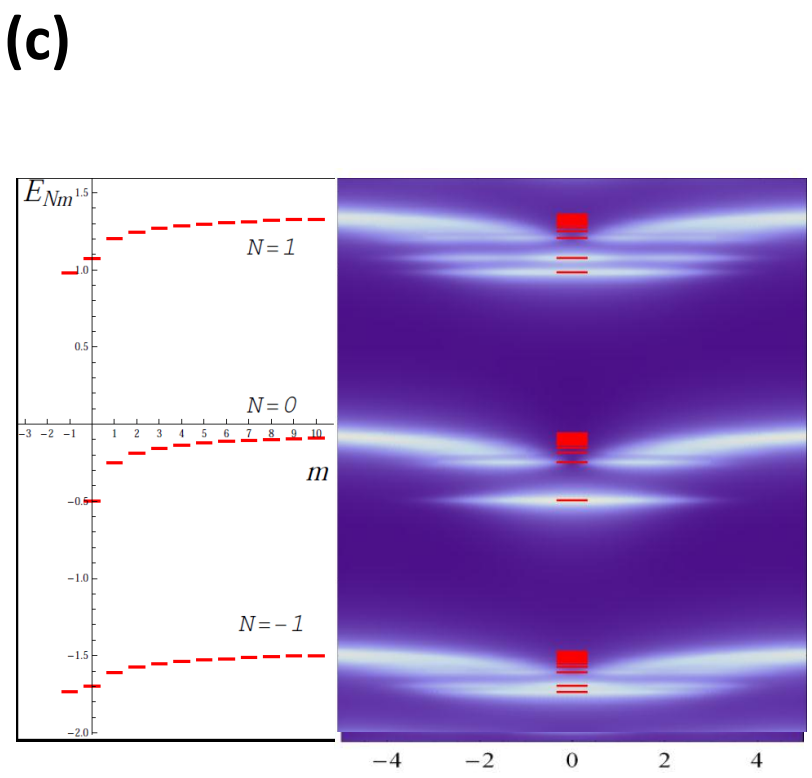
(c)
E_{Nm}
N = 1
N = 0
m
N = −1
−4 −2 0 2 4

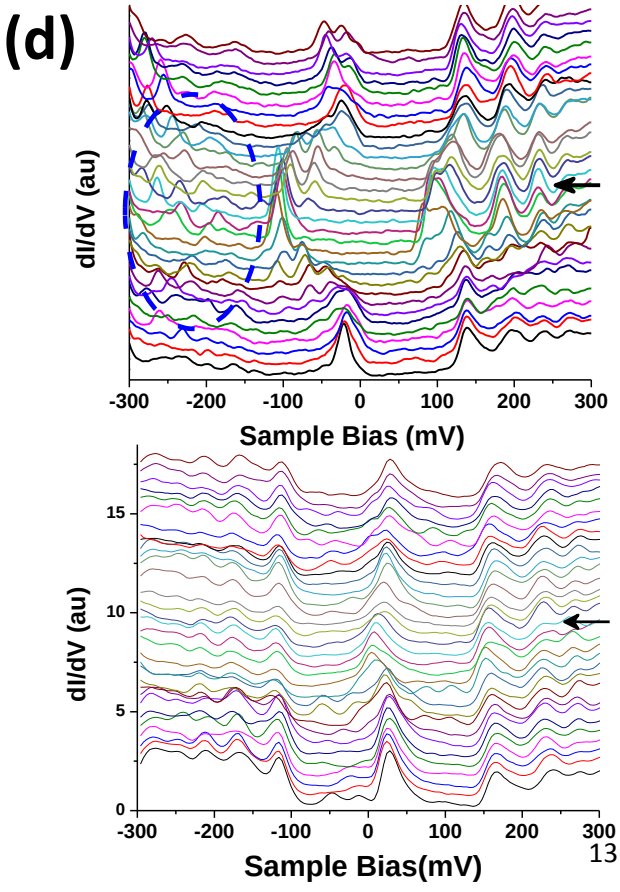
(d)
dI/dV (au)
-300 -200 -100 0 100 200 300
Sample Bias (mV)
dI/dV (au)
15
10
5
0
-300 -200 -100 0 100 200 300
Sample Bias(mV)

Figure 4

References

1 Dirac, P. A. M. The quantum theory of the electron. *Proc. R. Soc. Lond. A* **117** 610 (1928).

2 Zeldovich, Y. B. & Popov, V. S. Electronic structure of superheavy atoms. *Soviet Physics Uspekhi* **14**, 673 (1972).

3 Castro Neto, A. H., Guinea, F., Peres, N. M. R., Novoselov, K. S. & Geim, A. K. The electronic properties of graphene. *Reviews of Modern Physics* **81**, 109 (2009).

4 Morgenstern, M. Scanning tunneling microscopy and spectroscopy of graphene on insulating substrates. *Physica Status Solidi B* **248**, 2423 (2011).

5 Andrei, E. Y., Li, G. & Du, X. Electronic properties of graphene: a perspective from scanning tunneling microscopy and magneto-transport. *Reports on Progress in Physics* **75** 056501 (2012).

6 Shytov, A. V., Katsnelson, M. I. & Levitov, L. S. Atomic collapse and quasi–Rydberg states in graphene. *Physical Review Letters* **99**, 246802, doi:10.1103/PhysRevLett.99.246802 (2007).

7 Pereira, V. M., Nilsson, J. & Castro Neto, A. H. Coulomb Impurity Problem in Graphene. *Physical Review Letters* **99**, 166802 (2007).

8 Fogler, M. M., Novikov, D. S. & Shklovskii, B. I. Screening of a hypercritical charge in graphene. *Physical Review B* **76**, 233402 (2007).

9 Wang, Y. *et al.* Mapping Dirac quasiparticles near a single Coulomb impurity on graphene. *Nat Phys* **8**, 653-657 (2012).

10 Khveshchenko, D. V. Coulomb-interacting Dirac fermions in disordered graphene. *Physical Review B* **74**, 161402 (2006).

11 Chen, J. H. *et al.* Charged-impurity scattering in graphene. *Nat Phys* **4**, 377-381 (2008).

12 Wehling, T. O., Yuan, S., Lichtenstein, A. I., Geim, A. K. & Katsnelson, M. I. Resonant Scattering by Realistic Impurities in Graphene. *Physical Review Letters* **105**, 056802 (2010).

13 Das Sarma, S., Adam, S., Hwang, E. H. & Rossi, E. Electronic transport in two-dimensional graphene. *Reviews of Modern Physics* **83**, 407-470 (2011).

14 Goerbig, M. O. Electronic properties of graphene in a strong magnetic field. *Reviews of Modern Physics* **83**, 1193-1243 (2011).

15 Gamayun, O. V., Gorbar, E. V. & Gusynin, V. P. Magnetic field driven instability of a charged center in graphene. *Physical Review B* **83**, 235104 (2011).

16 Zhang, Y., Barlas, Y. & Yang, K. Coulomb impurity under magnetic field in graphene: A semiclassical approach. *Physical Review B* **85**, 165423 (2012).

17 Li, G., Luican, A. & Andrei, E. Y. Scanning Tunneling Spectroscopy of Graphene on Graphite. *Physical Review Letters* **102**, 176804 (2009).

18 Luican, A., Li, G. & Andrei, E. Y. Quantized Landau level spectrum and its density dependence in graphene. *Physical Review B* **83**, 041405(R) (2010).

19 Luican, A. *et al.* Single-Layer Behavior and Its Breakdown in Twisted Graphene Layers. *Physical Review Letters* **106**, 126802 (2011).

20 Dial, O. E., Ashoori, R. C., Pfeiffer, L. N. & West, K. W. High-resolution spectroscopy of two-dimensional electron systems. *Nature* **448**, 176-179 (2007).

21 D. S. Lee, C. R., T. Beringer, A. H. Castro Neto, K. von Klitzing, U. Starke, and J. H. Smet. Quantum Hall Effect in Twisted Bilayer Graphene. *Phys. Rev. Lett.* **107**, 216602 (2011).

22 Sanchez-Yamagishi, J. D. *et al.* Quantum Hall Effect, Screening, and Layer-Polarized Insulating States in Twisted Bilayer Graphene. *Physical Review Letters* **108**, 076601 (2012).

23 Yacoby, A., Hess, H. F., Fulton, T. A., Pfeiffer, L. N. & West, K. W. Electrical imaging of the quantum Hall state. *Solid State Communications* **111**, 1-13 (1999).
24 Niimi, Y., Kambara, H. & Fukuyama, H. Localized Distributions of Quasi-Two-Dimensional Electronic States near Defects Artificially Created at Graphite Surfaces in Magnetic Fields. *Physical Review Letters* **102**, 026803 (2009).
25 Yoshioka, D. Local Density of States around Impurity in a Strong Magnetic Field: I. Two-Dimensional System with Parabolic Dispersion. *Journal of the Physical Society of Japan* **76** (2009).
26 Miller, D. L. *et al.* Real-space mapping of magnetically quantized graphene states. *Nat Phys* **6**, 811-817 (2010).
27 Pyatkovskiy, P. K. & Gusynin, V. P. Dynamical polarization of graphene in a magnetic field. *Physical Review B* **83**, 075422 (2011).
28 Xue, J. *et al.* Scanning tunnelling microscopy and spectroscopy of ultra-flat graphene on hexagonal boron nitride. *Nat Mater* **10**, 282-285 (2011).